



End-to-End Differentiable Model for Optimization of Rocket-Powered Vehicles Including Plume Radiant Emission

Kelly J. Mathesius,^{*} Peter D. Sharpe,[†] and R. John Hansman[‡]
Massachusetts Institute of Technology, Cambridge, Massachusetts 02139

<https://doi.org/10.2514/1.A36168>

This paper proposes an end-to-end differentiable model for infrared radiant emission for low-altitude exhaust plumes. Considering plume radiant emission during the design phase is important for ensuring vehicle design constraints and objectives can be met while accounting for the coupling of plume radiant emission with other aspects of vehicle design. The model is suitable for computational frameworks using automatic differentiation or gradient-based optimizers—such as CasADi and AeroSandbox—which enable direct optimization of solid rocket-powered vehicle design with constraints on plume radiant emission. It consists of six submodels of different coupled physical phenomena: chamber thermodynamic equilibrium, motor internal ballistics, isentropic nozzle flow, plume flow field, afterburning kinetics, and radiative transfer. The combined model shows reasonable agreement for several different rocket-powered vehicles. The use of the model is demonstrated in an example case study for optimizing a low-thrust, transonic, rocket-powered aircraft concept.

Nomenclature

A	= area, m ²
a	= propellant burn rate coefficient, m · s ⁻¹ · Pa ⁻ⁿ
B	= reaction rate pre-exponential factor, (kmol · m ⁻³) ^{1-Σk} · s ⁻¹
b_{j0}	= initial system mass of element j , kg
C_D	= plume drag coefficient, -
C_F	= nozzle coefficient of thrust, -
c^*	= propellant characteristic velocity, m · s ⁻¹
d	= diameter (nozzle throat or plume), m
E_a	= activation energy, J · kg ⁻¹ · K ⁻¹
F	= thrust, N
f_v	= volume fraction, -
\hat{g}	= Gibbs free energy, J · mol ⁻¹
H_0	= initial system enthalpy, J
\hat{h}	= enthalpy, J · mol ⁻¹
I_λ	= spectral radiance, W · sr ⁻¹ · μm ⁻¹ · m ⁻²
$I_{b\lambda}$	= blackbody spectral radiance, W · sr ⁻¹ · μm ⁻¹ · m ⁻²
J_λ	= plume spectral radiant intensity, W · sr ⁻¹ · μm ⁻¹
k	= concentration exponents for reaction rate, -
L	= path length, m
l	= path, m
M	= Mach number, -
\hat{M}	= molecular or atomic mass, kg · mol ⁻¹
\dot{m}	= mass flow rate, kg · s ⁻¹
n	= propellant burn rate exponent, -, or number of moles, -
p	= pressure, Pa
q_1, q_2	= real, imaginary part of refractive index, -
R	= specific gas constant, J · kg ⁻¹ · K
\hat{R}	= ideal gas constant, J · mol ⁻¹ · K
r	= reaction rate, mol · m ⁻³ · s ⁻¹
\hat{s}	= entropy, J · mol ⁻¹ · K ⁻¹
T	= temperature, K
u	= velocity, m · s ⁻¹
v_{ij}	= number of moles of element j per mole of species i , -

Received 15 June 2024; revision received 8 August 2024; accepted for publication 6 September 2024; published online 25 October 2024. Copyright © 2024 by the authors. Published by the American Institute of Aeronautics and Astronautics, Inc., with permission. All requests for copying and permission to reprint should be submitted to CCC at www.copyright.com; employ the eISSN 1533-6794 to initiate your request. See also AIAA Rights and Permissions www.aiaa.org/randp.

*Graduate Researcher, Department of Aeronautics and Astronautics; kjmath@mit.edu (Corresponding Author).

†Graduate Researcher, Department of Aeronautics and Astronautics.

‡T. Wilson Professor in Aeronautics, Department of Aeronautics and Astronautics. Member AIAA.

w	= mole fraction, -
X	= stoichiometric coefficient, -
x	= distance downstream in plume, m
y	= mass fraction, -
α	= single line group model fine structure parameter, -
β	= entrainment coefficient, -
δ	= spectral line spacing, μm
ϵ	= nozzle expansion ratio, -
γ	= propellant exhaust gas ratio of specific heats, -
κ	= absorption coefficient, m ⁻¹
λ	= wavelength, μm, or Lagrange multiplier, -
η	= wavenumber (inverse of wavelength), cm ⁻¹
ϑ	= species production rate coefficient, -
$\dot{\omega}$	= species production rate, kg · m ⁻³ · s ⁻¹
ρ	= density, kg · m ⁻³
σ	= broadening half-width, μm
τ	= time constant, s, or optical depth, -

Subscripts

b	= burning surface
C	= collision broadening
c	= combustion
D	= Doppler broadening
e	= exit
i	= species
j	= chemical element
p	= solid propellant
t	= throat
x	= station in plume
λ	= spectral quantity (wavelength-dependent)
η	= spectral quantity (wavenumber-dependent)
0	= start of plume
∞	= ambient

Superscripts

0	= standard conditions
$^\wedge$	= molar quantity

I. Introduction

A. Motivation for Model Development

FOR applications where vehicle visibility is a concern, exhaust plume radiant emission is an important aspect of solid rocket-powered vehicle performance. However, it is often not considered during the design phase or in design optimization studies, despite significant physical couplings with other vehicle disciplines, especially

propulsion. Typical modeling approaches are computationally expensive and rely on CFD and complicated integration schemes that are not well-suited for rapid design iteration or design optimization.

To address these modeling gaps, an end-to-end differentiable model for exhaust plume radiant emission was developed. This model captures the effects of several key rocket-powered vehicle design parameters on the spatially integrated exhaust plume spectral radiant intensity. The model is compatible with computational frameworks using automatic differentiation or gradient-based optimizers, which enables scalable design optimization including many variables without having to sweep the entire design space. The AeroSandbox aircraft design optimization framework, which is described further in Sec. II, is specifically used in this work for implementing the model and leveraging it for vehicle design optimization [1]. This model enables design optimization for vehicles including constraints on plume spectral radiant intensity and its integration with all existing aircraft design models in AeroSandbox.

B. Previous Work in Exhaust Plume Radiant Emission Modeling

A rocket exhaust plume is the formation of hot, high-velocity combustion products that exit the nozzle of a rocket. The hot gases and condensed particles (if present) in an exhaust plume radiate thermal energy, producing a characteristic plume spectral radiant emission signature for a particular propulsion system. Many previous studies have developed methods for modeling exhaust plume radiant emission for rocket-powered vehicles [2–10]. Most studies use the same overarching approach, which typically involves models for the combustion chamber, nozzle and exhaust flow field, and plume radiative transfer. Woodroffe concluded that the effects of radiation on the exhaust flow field energy calculations are small and that the exhaust flow field and plume radiative transfer can be treated as uncoupled and modeled in series [11]. This treatment is used by several radiant emission studies [2,10,12].

Given the high temperatures and pressures in the combustion chamber, standard practice for determining combustion chamber properties such as temperature and species mass fractions is to use a thermodynamic equilibrium model. Thermodynamic equilibrium models are used by many studies in the literature as part of exhaust plume radiant emission modeling studies [2–8,10].

Most studies use 2D-axisymmetric CFD to determine properties throughout the exhaust flow field [2–9]. Alternatively, a simplified 1D exhaust plume flow field model originally proposed by Woodroffe [11], which captures the key effects of turbulent entrainment, jet expansion, and freestream flow, was used by a few studies with reasonable results [10,13,14]. Afterburning kinetics is coupled with the exhaust flow field calculations. Chemical reactions are modeled as either reversible elementary reactions or three-body reactions. Different reaction mechanisms and chemical species are modeled in different radiant emission modeling studies, although they typically account for 10 to 30 reactions [2–10].

Spectral properties of the radiating gaseous species in the plume are modeled with line-by-line, narrow band, or wide band models [15]. Narrow band models are used most frequently, as they represent a good balance between simplicity and accuracy. Many studies use the *single line group* narrow band model developed by Ludwig et al., which uses a functional relation for the optical depth at different temperatures and wavelengths [16]. The plume spectral radiance and radiant intensity are found by integrating the radiative transfer equation. For nonscattering plumes, relatively simple line-of-sight methods are often used for integrating the radiative transfer equation [2,8,10]. Finite volume, discrete ordinates, or other discretization methods are also used by several studies, which are more complex but enable the effects of scattering to be included [5–7,9].

This work focuses on exhaust plume radiant intensity modeling that is compatible with automatic differentiation and gradient-based optimizers, which to the authors' knowledge has not been previously attempted in studies in the open literature. The models in this work are implemented using the AeroSandbox design optimization framework, which is described further in the next section. The modeling approach focuses on using simple models that capture the core

physics coupling rocket-powered vehicle design parameters to exhaust plume radiant emission, drawing from many of the previously discussed modeling methods. It uses no black-box codes, and surrogate models are developed where appropriate. This model enables direct computational optimization of rocket-powered vehicle design parameters such as propellant formulation or mixture ratio, nozzle throat diameter, and chamber pressure with constraints on plume radiant intensity.

II. Design Optimization with AeroSandbox Computational Framework

A. AeroSandbox Overview

The model presented in this work was specifically developed to be compatible with automatic differentiation and gradient-based computational optimization frameworks. The AeroSandbox optimization framework was used for implementing the model in this work, which is a python computational framework for high-dimensionality conceptual aircraft design optimization developed by Sharpe [1]. AeroSandbox solves design problems using CasADi [17], a framework for automatic differentiation, and IPOPT [18], a robust gradient-based optimizer for nonlinear programming. Automatic differentiation is a method for evaluating computational function derivatives by decomposing functions into elementary functions which have known derivatives and then combining those derivatives using the chain rule [19]. Automatic differentiation can be used to compute derivatives for gradient-based optimizers such as IPOPT and provides a computationally efficient method for AeroSandbox and other packages to solve high-dimensional engineering problems.

This work extended the existing AeroSandbox models for aircraft design to incorporate models for solid rocket motor exhaust plume radiant emission. This subsequently enables radiant emission to be coupled with all of the existing tools and models for aircraft design optimization already available in AeroSandbox.

B. Model Limitations

Despite its great flexibility, the AeroSandbox framework creates some limitations on the types of models that can be used. The most important of these limitations are described subsequently:

1) *Glass-box models*: to evaluate derivatives using automatic differentiation, AeroSandbox needs direct access to the code for the model. Therefore, models in AeroSandbox must be *glass-box* and coded directly in python using AeroSandbox.numpy syntax; *black-box* codes cannot be used.

2) C^1 -continuity: AeroSandbox uses gradient descent with automatic differentiation to solve optimization problems, which requires that models be C^1 -continuous with respect to any problem variables. AeroSandbox has several tools for implementing surrogate models to meet the C^1 -continuity requirement, which are described later in this section.

3) *Nonstiff differential equations*: AeroSandbox integrates ODEs using a trapezoidal collocation method, which enforces integration as constraints between time steps assuming a trapezoidal integration scheme with nonadaptive time steps. The constraints defined with the trapezoidal scheme are solved implicitly with IPOPT in AeroSandbox. This integration scheme does not converge well for some stiff systems of differential equations, and therefore stiff equations should be implemented with caution.

C. Surrogate Modeling Tools

AeroSandbox has a number of tools for developing differentiable models from otherwise discontinuous models. Piece-wise models can be blended using a sigmoid transition function, which is implemented in AeroSandbox with the AeroSandbox.numpy.blend() method. Models based on data points can be interpolated using a differentiable spline. In AeroSandbox, structured data can be modeled using the InterpolatedModel() class, and unstructured data can be modeled using the UnstructuredInterpolatedModel() class.

III. End-to-End Differentiable Model Overview and Implementation

Six submodels of different coupled physical phenomena were developed and implemented to predict exhaust plume radiant intensity. The submodels and the couplings between them are depicted in Fig. 1. The approach for each submodel was chosen as a balance between accuracy and simplicity: the simplest possible model was chosen that captured the necessary core physics for conceptual design and maintained compatibility with the AeroSandbox modeling limitations discussed in Sec. II. It should be noted that this simplified approach is suitable for predicting exhaust plume radiant intensity—a quantity integrated over the entire exhaust plume, and is the focus of this modeling effort—and is not intended for evaluating spatially resolved radiant quantities.

A. Chamber Thermodynamic Equilibrium

Propellant combustion temperature and product species fractions are calculated in the chamber thermodynamic equilibrium model. These propellant combustion properties are determined in this model using equilibrium thermodynamics. Namely, combustion temperature and products are determined by minimizing their Gibbs free energy subject to conservation of mass and enthalpy. Which species to include in the combustion products is simply guessed at using the common combustion products for solid rocket propellants (and species that are not present will simply solve to near-zero mole fractions). The governing equations for the chamber thermodynamic equilibrium module are given subsequently [20]:

Minimization of Gibbs free energy for gaseous products:

$$\hat{g}_i^0(T_c) + \hat{R}T_c \ln\left(\frac{n_i}{n_{\text{gas}}}\right) + \hat{R}T_c \ln\left(\frac{p_c}{p_0^0}\right) - \sum_{j=1}^{N_{\text{elements}}} \lambda_j v_{ij} = 0 \quad \text{for } i = 1, \dots, N_{\text{species}} \quad (1)$$

Conservation of mass of chemical elements:

$$\sum_{i=1}^{N_{\text{species}}} v_{ij} n_i - \frac{b_{j0}}{\hat{M}_j} = 0 \quad \text{for } j = 1, \dots, N_{\text{elements}} \quad (2)$$

Conservation of enthalpy:

$$\sum_{i=1}^{N_{\text{species}}} n_i \hat{h}_i^0 - H_0 = 0 \quad (3)$$

Enforce that n_{gas} is the molar sum of gaseous products:

$$\sum_{i=1}^{N_{\text{species}}} n_i - n_{\text{gas}} = 0 \quad (4)$$

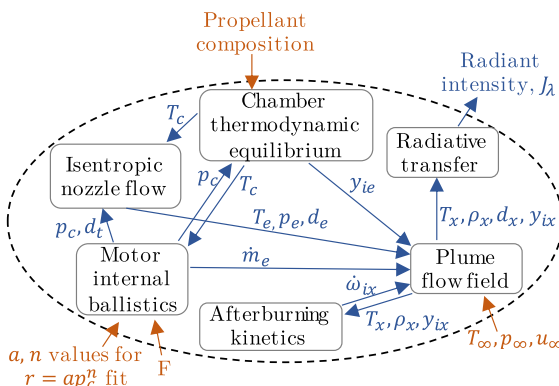


Fig. 1 Submodels and couplings in the end-to-end differentiable plume model.

This formulation of the chamber thermodynamic equilibrium problem was validated by Ponomarenko [20], who obtained perfect agreement with NASA CEARUN [21] for six different test cases.

Lagrange multipliers λ_i are used, following the formulation given by Ponomarenko [20]. Using Lagrange multipliers allows the thermodynamic equilibrium problem to be solved as a system of constrained equations, rather than as a true minimization problem. This is important for implementation in AeroSandbox, so that the equations can be implemented as a set of problem constraints, rather than as a minimization which would be implemented as part of the problem objective.

Gibbs free energy is calculated using $\hat{g}_i^0 = \hat{h}_i^0 - T_c \hat{s}_i^0$. Species thermodynamic properties—namely, molar enthalpy \hat{h}^0 and molar entropy \hat{s}^0 —are determined using the NASA 9-coefficient polynomial parameterizations [21].

B. Internal Ballistics and Nozzle Flow

The internal ballistics module calculates motor equilibrium mass flow, chamber pressure, and thrust. It requires chamber temperature as an input, as well as properties of the propellant, including propellant solid density ρ_p , and a and n values to characterize the propellant using the typical empirical burn rate law $r_p = ap_c^n$. Nozzle flow is calculated using standard 1D isentropic nozzle flow theory. Equilibrium chamber pressure is calculated using [22]:

$$p_c = (K_n \rho_p c^* a)^{1/(1-n)}; \quad K_n \equiv \frac{A_b}{A_t} \quad (5)$$

and equilibrium thrust is calculated using [22]:

$$F = p_c^n C_F \left(\frac{p_c}{p_e}, \frac{p_\infty}{p_e}, \gamma \right) c^*(R, \gamma, T_c) a \rho_p A_b \quad (6)$$

The previously given equations are implemented using the proptools python library and have been validated with a large number of test cases published in the library's documentation [23]. The nozzle flow module calculates flow properties at the nozzle exit—including nozzle exit temperature, velocity, and area—using isentropic flow equations.

C. Plume Flow Field

I. Governing Equations

The plume flow field module calculates temperature, density, velocity, and species mass fractions throughout the exhaust plume. A 1D simplified plume flow field model is used to determine the temperature, density, velocity, diameter, and species mass fractions throughout the exhaust plume. The model, originally proposed by Woodroffe [11], and used more recently by Niu et al. [10], Simmons [13], and Mao et al. [14], makes the following assumptions:

1) plume properties are averaged at each axial station (i.e., no radial variations in plume properties);

2) entrained mass is mixed instantly and uniformly through the plume cross section;

3) pressure in the plume is constant and equal to ambient pressure;

4) nozzle expansion is near perfect, such that the plume initial expansion region is small and can be neglected; and

5) radiation from the plume has no influence on the flow parameters throughout the plume.

This 1D plume flow field model concept is illustrated subsequently in Fig. 2. After the flow exits the nozzle, there is an initial expansion region where the exhaust flow expands to ambient pressure. Once ambient pressure is achieved in the plume, the plume enters the turbulent mixing region, where it begins mixing and reacting with air from the freestream.

The governing equations for the 1D plume flow field model enforce conservation of mass, momentum, energy, and species flows, in addition to the ideal gas law state equation. These equations are given subsequently.

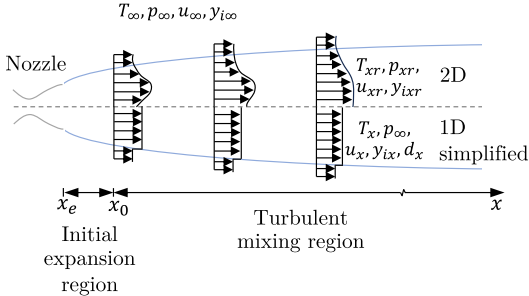


Fig. 2 Comparison of 1D simplified and 2D plume flow field model.

Mass flow:

$$\frac{d}{dx}(\rho d^2 u) = 4d\beta \sqrt{\rho \rho_\infty} (u - u_\infty) \quad (7)$$

Momentum flow:

$$\frac{d}{dx}(\rho d^2 u^2) = u_\infty \frac{d}{dx}(\rho d^2 u) \quad (8)$$

Energy flow[§]:

$$\frac{d}{dx} \left[\rho d^2 u \left(h + \frac{1}{2} u^2 \right) \right] = \left(h_\infty + \frac{1}{2} u_\infty^2 \right) \frac{d}{dx}(\rho d^2 u) \quad (9)$$

Species flow:

$$\frac{d}{dx}(\rho d^2 u y_i) = y_{i\infty} \frac{d}{dx}(\rho d^2 u) + \dot{\omega}_i d^2 \quad (10)$$

Ideal gas law:

$$p_\infty = \rho R T \quad (11)$$

In section 5.6 of Ref. [13], the outputs of this 1D flow field model, in conjunction with a simple radiative transfer model, were compared to experimental radiance data for short- and mid-wave infrared bands for a Titan IIC and Titan II plume. Both plumes showed reasonable agreement between the station irradiance data and model results for downstream distances of 0 to 3 km.

2. Initial Conditions

The initial conditions proposed by Mao et al. [14] are used in this module, which assume frozen flow and no entrainment effects in the plume initial expansion region. The following system of equations can be solved to determine the initial conditions at the start of the turbulent mixing region x_0 :

Mass flow:

$$\rho_0 u_0 d_0^2 = \rho_e u_e d_e^2 \quad (12)$$

Momentum flow:

$$\rho_0 u_0^2 d_0^2 = \rho_e u_e^2 d_e^2 + (p_e - p_\infty) d_e^2 + \frac{1}{2} C_D \rho_\infty u_\infty^2 d_0^2 \quad (13)$$

Energy flow:

$$h_0 + \frac{1}{2} u_0^2 = h_e + \frac{1}{2} u_e^2 \quad (14)$$

[§]For self-consistency, the energy flow equation is written differently here than how it is written by Woodroffe [11]. Namely, a term on the right-hand side accounting for the heat released due to afterburning reactions is omitted, because the heat release is accounted for by the heat of formation already included in the definition of enthalpy.

Species flow:

$$y_{0i} = y_{ei} \quad (15)$$

where

$$C_D = \frac{16}{9\pi} \left\{ \left[\left(1 - \left(\frac{p_e}{p_c} \right)^{(y-1)/y} \right)^{1/2} + \frac{\epsilon(p_e - p_\infty)}{p_c C_{F,\max}} \right]^{-1} - 1 \right\} \quad (16)$$

$$C_{F,\max} = \left[\frac{2\gamma^2}{\gamma-1} \left(\frac{2}{\gamma+1} \right)^{(\gamma+1)/(\gamma-1)} \right]^{1/2} \quad (17)$$

In the previously given equations, subscript e refers to conditions at the nozzle exit, subscript 0 refers to conditions at the start of the turbulent mixing region, C_D is the plume drag coefficient, $C_{F,\max}$ is the maximum thrust coefficient, ϵ is the nozzle expansion ratio, and γ is the ratio of specific heats.

3. Enthalpy

Enthalpy h [$J \cdot kg^{-1}$] of the gas mixture is calculated as a weighted sum of the enthalpies of the constituent species:

$$h = \sum_{i=1}^{\text{species}} y_i \hat{h}_i^0 \quad (18)$$

where y_i is species mass fraction, \hat{M}_i is species molecular weight, and \hat{h}_i^0 is the species molar enthalpy, which can be calculated using the NASA 9-coefficient polynomials [21].

4. Entrainment Coefficient

The entrainment coefficient β is determined using the fits developed by Witze [24]. The fits propose different values for β for subsonic and supersonic flows. Assuming that the flow at the start of the turbulent mixing region is supersonic, the expressions for entrainment coefficient for the supersonic and subsonic portions of the plume are

$$\beta = \begin{cases} 0.063(M_0^2 - 1)^{-0.15} & \text{for } M \geq 1 \\ 0.0672 \left(\frac{\rho_\infty}{\rho_0} \right)^{-0.22} & \text{for } M < 1 \end{cases} \quad (19)$$

where M is the Mach number and M_0 is the Mach number at the start of the turbulent mixing region x_0 . The two regions are blended together using the `AeroSandbox.numpy.blend()` method introduced in Sec. II.C.

5. Soot

The following assumptions are made when calculating the soot concentrations and temperatures in the plume flow field:

1) soot in the plume is assumed nonreactive after it exits the nozzle, such that the mass flow rate of soot at any station in the plume is constant and equal to the mass flow rate of soot at the nozzle exit;

2) the soot mass fraction is assumed to be small, such that its presence does not affect local plume temperatures, velocities, or gas densities;

3) the soot particles in the plume are assumed small, such that soot in the plume has the same temperature and velocity as the local flow; and

4) there are no radial variations in soot concentration in the plume. Following these assumptions, the soot volume fraction $f_{v,\text{soot}}$ throughout the plume is determined using

$$f_{v,\text{soot}} = y_{0,\text{soot}} \frac{\dot{m}_0}{\dot{m}} \frac{\rho}{\rho_{\text{soot}}} \quad (20)$$

where subscript 0 represents conditions at the start of the turbulent mixing region, \dot{m} is mass flow rate, ρ is density in the plume, and ρ_{soot} is the solid density of carbon soot.

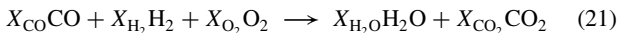
D. Afterburning Kinetics

Finite rate reaction mechanisms typically used to evaluate afterburning reaction kinetics in exhaust plumes (such as those used by Niu et al. [10] or Mao et al. [14]), are extremely stiff and difficult to integrate without specialized integrators. The integration scheme used by AeroSandbox (see Sec. II.B) is not well suited for stiff systems of equations and cannot reliably integrate a detailed chemical kinetics mechanism. To make the reaction kinetics more computationally tractable in AeroSandbox, a reduced-order global reaction mechanism kinetics model was developed. The model was developed with the goal of finding the simplest model for afterburning kinetics that captures the core physics and limiting behavior and scales correctly. This model is not meant to be an equally rigorous replacement for detailed reaction rate mechanisms, but rather a simplified and practical tool for supporting conceptual level design and analysis of exhaust plumes.

The model assumes a global reaction mechanism with a single reaction rate. All fuel species are consumed at the same rate (relative to their initial quantities in the plume). An Arrhenius type rate equation is used to determine the reaction rate, with parameters fitted to results from a more detailed reaction mechanism. This removes the dependence of the afterburning kinetics model on reaction pathways involving small concentrations of minor species and focuses on bulk conversion of fuel species into product species. When added as a constraint to the larger plume model in AeroSandbox, it enables solver convergence more readily than traditional finite rate reaction schemes. More details of the model are provided in the following subsections.

1. Global Reaction Mechanism

A global reaction mechanism is assumed:



where X_i represents the stoichiometric coefficients for each species i . The global reaction is assumed to be irreversible, HCl is assumed to be nonreactive, and reactions involving other species are ignored.

Appropriate stoichiometric coefficients X_i must be determined so that the reaction mechanism is balanced. The stoichiometric coefficients for the fuel species (CO and H₂) are taken as their respective initial mole fractions w_{ei} at the nozzle exit. The stoichiometric coefficients for O₂ and the product species can be calculated as a function of the coefficients for the fuel species to ensure the mechanism is balanced. The equations for calculating these coefficients are as follows:

$$\begin{aligned} X_{\text{CO}} &= w_{e,\text{CO}} \\ X_{\text{H}_2} &= w_{e,\text{H}_2} \\ X_{\text{O}_2} &= \frac{1}{2}X_{\text{CO}} + \frac{1}{2}X_{\text{H}_2} \\ X_{\text{H}_2\text{O}} &= X_{\text{H}_2} \\ X_{\text{CO}_2} &= X_{\text{CO}} \end{aligned} \quad (22)$$

2. Global Reaction Rate Equation

The global reaction mechanism leads to a global reaction rate r (units: mol · m⁻³ · s⁻¹) such that the species production rate $\dot{\omega}_i$ (units: kg · m⁻³ · s⁻¹) can be defined as

$$\dot{\omega}_i \equiv \vartheta_i \hat{M}_i r \quad (23)$$

where subscript i represents species, $\vartheta_i = -X_i$ for reactant species, $\vartheta_i = +X_i$ for product species, and \hat{M}_i is the molecular weight.

The global reaction rate r is assumed to have an Arrhenius equation form, similar to what is used to model elementary reactions in detailed reaction mechanisms:

$$r = Be^{-E_a/RT}[\text{fuel}]^{k_{\text{fuel}}}[\text{O}_2]^{k_{\text{O}_2}}[\text{gas}]^{k_{\text{gas}}} \quad (24)$$

where B is the pre-exponential factor, T is the temperature, E_a is the reaction activation energy, R is the universal gas constant, k represents concentration exponents, and bracketed quantities are concentrations. The concentration of fuel [fuel] includes CO and H₂ (i.e., [fuel] = [CO + H₂]). The general gas concentration term (the final term in the equation, [gas] ^{k_{gas}}) allows for effects of third-body reactions to be captured in the reaction rate model.

3. Global Reaction Rate Parameter Fits

The parameters B , E_a , k_{fuel} , k_{O_2} , and k_{gas} are fitted using a more detailed reaction kinetics mechanism implemented using the python package Cantera [25]. Specifically, the 28 reaction, 13 species mechanism recommended by Ecker et al. 2019 [26], which was intended for combustion modeling in solid rocket motor plumes, is used to fit the model parameters. Ecker et al. validated their model against other published kinetics models and experimental data for several different reactions and demonstrated good agreement [26].

Reactions for combinations of initial temperatures between 600 and 3000 K, pressures between 0.1 and 1 atm, and exhaust-to-air mass ratios[¶] (EARs) between 0.01 and 100 were simulated in an ideal gas constant pressure and temperature reactor in Cantera. The large range of exhaust-to-air ratios is chosen to account for different conditions throughout the plume: near the nozzle exit, little air is yet to be entrained, so the gas mixture is fuel rich and EAR $\gg 1$; far away from the nozzle exit, much more air has been entrained than initial exhaust flow, so the mixture is fuel lean and EAR $\ll 1$. The relative ratios of fuel species are chosen to match the equilibrium combustion products of an ammonium perchlorate composite propellant consisting of 80% ammonium perchlorate and 20% hydroxyl-terminated polybutadiene based binder, which is described further in Ref. [27].

For each simulated reaction, the concentration of O₂ versus time is recorded, along with initial concentrations of all species and the equilibrium concentration of O₂. An exponential decay model $[O_2] - [O_2]_{\text{equilibrium}} = ([O_2]_{t=0} - [O_2]_{\text{equilibrium}})e^{-t/\tau}$ is fit to the O₂ concentration versus time data using the lmfit python package [28]. The reaction rate for O₂ is taken to be the derivative of the fitted model at $t = 0$, or $r_{O_2} = -([O_2]_{t=0} - [O_2]_{\text{equilibrium}})/\tau$. The value of r_{O_2} is recorded for each combination of pressure and EAR. The global reaction rate r is taken as $r = r_{O_2}/\vartheta_{O_2}$.

The simulated global reaction rate r was fit to the global reaction rate model given in Eq. (24) also using lmfit. A low-temperature and high-temperature regime is apparent in the reaction rate values r , so the reaction rate equation given in Eq. (24) is fit to r separately for these two regimes, and the results are blended together using the AeroSandbox.numpy.blend() method described in Sec. II.C. The low-temperature regime reaction rate values r are evaluated using temperatures from 600 to 800 K, and the high-temperature regime values are evaluated using temperatures from 1000 to 3000 K. The fitted parameters for the two regimes are given in Table 1. The fitted reaction rate model is plotted versus temperature for a number of exhaust-to-air ratios and pressures in Fig. 3, along with the values for r determined using the previously given methods. The model shows reasonable agreement with the Cantera outputs and captures the scaling and limiting behavior of temperature, pressure, and initial mole fractions on afterburning reaction rate. This model should only be used for pressures > 0.1 atm. At pressures below this, the assumption of irreversible reactions discussed in Sec. III.D.1 breaks down, and the global reaction rate model given in Eq. (24) is no longer a good fit for evaluating the reaction rate.

A comparison of the species mole fractions for several test cases evaluated using the Ecker et al. mechanism and the simplified global reaction rate model is shown in Fig. 4. The Ecker et al. mechanism was evaluated using Cantera. The temperature was held constant for both

[¶]Exhaust-to-air ratios have an approximately linear relationship with equivalence ratio, defined as $\phi \equiv (w_{\text{fuel}}/w_{\text{O}_2})/(w_{\text{fuel}}/w_{\text{O}_2})_{\text{stoich}}$. They have values of the same order of magnitude for propellants in this work as well: for instance, for the combustion products of the baseline propellant formulation at stoichiometric conditions, $\phi = 1$ (by definition) and EAR = 0.69.

Table 1 Parameters for the global reaction rate model

	Low-temperature	High-temperature
$B [(\text{kmol} \cdot \text{m}^{-3})^{1-\sum k} \cdot \text{s}^{-1}]^a$	9.641×10^{12}	1.580×10^{11}
$E_a/R [\text{K}]$	24834	9756
$k_{\text{fuel}} [-]$	1.403	1.861
$k_{\text{O}_2} [-]$	0.652	1.793
$k_{\text{gas}} [-]$	-0.471	-1.621

^aThe pre-exponential factor B must have the appropriate units so that the reaction rate r has the correct units of $\text{kmol} \cdot \text{m}^{-3} \cdot \text{s}^{-1}$. The units for B account for the concentration terms in the reaction rate equation, where $\sum k = k_{\text{fuel}} + k_{\text{O}_2} + k_{\text{gas}}$.

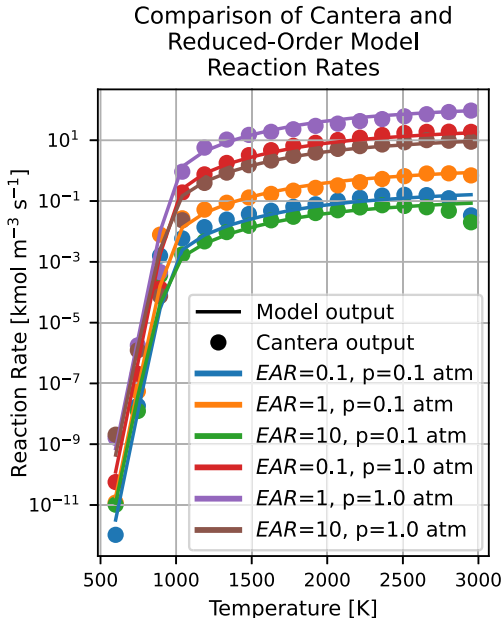


Fig. 3 Comparison of Cantera and fitted global reaction rate model outputs.

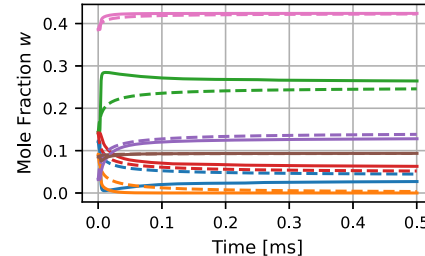
models in these comparisons, because the global reaction rate model is only meant to evaluate species production rates, and the temperature calculation is handled by the plume flow field model presented in Sec. III.C.1. Despite its simplicity, the global reaction rate model generally captures the species behavior for a range of temperatures, pressures, and exhaust-to-air ratios. The steady-state mole fractions are very similar between both models, as are the timescales of species mole fraction evolution. The global model does appear to slightly underpredict conversion of H_2 to H_2O and overpredict conversion of CO to CO_2 . However, because to first order the species optical depth scales linearly with species mole fraction, this model is still useful and acceptable for understanding the scaling of afterburning reactions in conceptual level analysis of solid rocket motor exhaust plumes.

E. Radiative Transfer

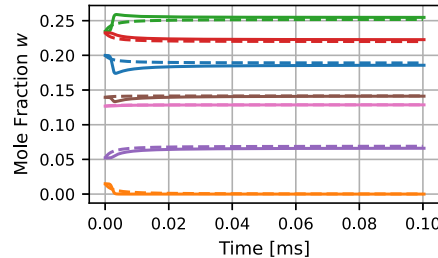
The plume spectral radiant intensity is evaluated in the radiative transfer submodel. It uses the temperature, density, and species distributions determined by the plume flow field module to determine the plume optical depth, integrate the radiative transfer equation, and subsequently determine the plume radiant emission properties. It should be noted that the radiative transfer model does not account for atmospheric absorption and should only be used for considering radiant emission without these effects.

1. Radiative Transfer Equation

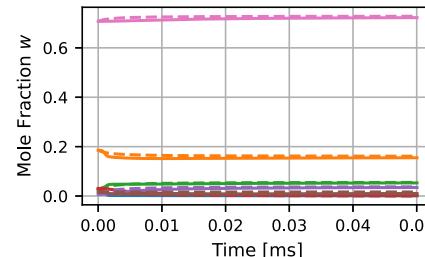
For simplicity in this study, the plume is assumed nonscattering and the viewing angle is assumed orthogonal to the plume axis of symmetry. Because the plume flow field model already assumes no



a) $T = 1500 \text{ K}$, $p = 1\text{E}+06 \text{ Pa}$, $\text{EAR} = 1$, exhaust = 0% oxamide



b) $T = 2000 \text{ K}$, $p = 1\text{E}+06 \text{ Pa}$, $\text{EAR} = 10$, exhaust = 0% oxamide



c) $T = 2500 \text{ K}$, $p = 5\text{E}+05 \text{ Pa}$, $\text{EAR} = 0.1$, exhaust = 8% oxamide

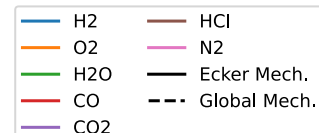


Fig. 4 Comparisons of species mole fractions for Ecker et al. and simplified global reaction mechanisms at constant temperature and pressure.

radial variations in flow properties in the plume (see Sec. III.C.1), and if the plume is viewed orthogonal to its axis of symmetry, then at any downstream station in the plume, the absorption coefficient κ_λ along the line of sight is constant, and the optical depth can be determined simply using $\tau_\lambda = \kappa_\lambda L$, where L is the path length through the plume. Following these assumptions, the radiant intensity along a line of sight is computed for this work using the well-known form of the radiative transfer equation for an isothermal, nonscattering medium:

$$I_\lambda = I_{b\lambda}(1 - e^{-\tau_\lambda}) \quad (25)$$

2. Plume Spatial Integration

The plume radiant intensity is found by integrating the spectral radiance I_λ over the projected area of the plume visible from the viewing location. Because the spectral radiant intensity J_λ is a spatial integration of spectral radiance I_λ along every line-of-sight in the plume, it is dependent on the plume flow field and spectral radiance values at every location in the plume. Determining the derivatives of J_λ with automatic differentiation in AeroSandbox is computationally expensive because of this dense dependence on the many variables throughout the exhaust plume. Therefore, some assumptions are made to simplify the spatial integration of the plume. The physical

path length $L(x)$ through the plume at each downstream location in the plume x is assumed constant and set as $0.95d(x)$ following the mean beam length approximation [29]. This allows a single value of $\tau_{\lambda i}$ to be calculated at each location x . The effective projected plume height at each station is taken as $0.95d(x)$ at each station as well. With these assumptions, the spectral radiant intensity can be evaluated as an integration along the x direction only:

$$J_{\lambda} = \int_x I_{\lambda}(x) 0.95d(x) dx \quad (26)$$

3. Optical Depth for Soot

The soot particles in the plume are assumed small enough such that scattering is negligible and the absorption coefficient can be calculated using [15]

$$\kappa_{\lambda, \text{soot}} = \frac{36\pi q_1 q_2}{(q_1^2 - q_2^2 + 2)^2 + 4q_1^2 q_2^2} \frac{f_{v, \text{soot}}}{\lambda} \quad (27)$$

where $f_{v, \text{soot}}$ is the volume fraction of soot, q_1 is the real part of the refractive index, q_2 is the imaginary part of the refractive index, and λ is the wavelength. The soot volume fraction $f_{v, \text{soot}}$ is calculated using Eq. (20). The refractive indices q_1 and q_2 are determined using the fits given by Chang and Charalampopoulos for wavelengths in the range of 0.4 to 30 μm [30]:

$$q_1 = 1.811 + 0.1263 \ln \lambda + 0.0270 \ln^2 \lambda + 0.0417 \ln^3 \lambda \quad (28)$$

$$q_2 = 0.5821 + 0.1213 \ln \lambda + 0.2309 \ln^2 \lambda - 0.0100 \ln^3 \lambda \quad (29)$$

where the wavelength λ is in micrometers. Following the assumptions made to integrate the radiative transfer equation in Sec. III.E.1, the optical depth due to soot absorption is simply $\tau_{\lambda, \text{soot}} = \kappa_{\lambda, \text{soot}} L$, where L is the path length through the plume.

4. Optical Depth for Molecular Gases

The optical depth τ_{λ} for molecular gases is determined using the *single line group* (SLG) model proposed by Ludwig et al. [16], which is used by several other studies in the exhaust plume radiant emission modeling literature [2–4, 10]. The single line group model is a narrow band model that proposes that the optical depth for a mixture of molecular gases in some small wavelength band is ultimately a function of gas temperature, gas pressure, species mass fractions, wavelength, and gas path:

$$\tau_{\lambda} = f(T, p, w_i, \lambda, l) \quad (30)$$

The SLG model is derived from a random Goody narrow band model for absorption coefficient with a hybrid Doppler-collision line shape. For each gas species, the SLG model calculates optical depth due to collision broadening $\tau_{C\lambda i}$ and the optical depth due to Doppler broadening $\tau_{D\lambda i}$ separately:

$$\tau_{C\lambda i} = \tau_{\lambda i}^* \left(1 + \frac{\tau_{\lambda i}^*}{4\alpha_{C\lambda i}} \right)^{-(1/2)} \quad (31)$$

$$\tau_{D\lambda i} = 1.7 a_{D\lambda i} \left(\ln \left[1 + \left(\frac{\tau_{\lambda i}^*}{1.7\alpha_{D\lambda i}} \right)^2 \right] \right)^{1/2} \quad (32)$$

where $\tau_{\lambda i}^*$ is the optical depth in the linear (optically thin) limit, $\alpha_{C\lambda i}$ is the fine structure parameter for collision broadening, and $\alpha_{D\lambda i}$ is the fine structure parameter for Doppler broadening. Simplifying the SLG model for a homogenous, isothermal path (the same assumptions made for the integration of the radiative transfer equation in Sec. III.E.1), $\tau_{\lambda i}^*$, $\alpha_{C\lambda i}$, and $\alpha_{D\lambda i}$ are calculated using

$$\tau_{\lambda i}^* = \bar{\kappa}_{\lambda i} L; \quad \bar{\kappa}_{\lambda i} = \bar{\kappa}_{\lambda i 0} \frac{p}{p^0} \frac{T^0}{T} \quad (33)$$

$$\alpha_{C\lambda i} = \frac{\sigma_{Ci}}{\delta_{\lambda i}} \quad (34)$$

$$\alpha_{D\lambda i} = \frac{\sigma_{D\lambda i}}{\delta_{\lambda i}} \quad (35)$$

where $\bar{\kappa}_{\lambda i}$ is the mean absorption coefficient, $\bar{\kappa}_{\lambda i}^0$ is the mean absorption coefficient at standard temperature and pressure, $1/\delta_{\lambda i}$ is the average line density, σ_{Ci} is the collision broadening half-width, $\sigma_{D\lambda i}$ is the Doppler broadening half-width, and L is the physical path length. Surrogate models for determining $\bar{\kappa}_{\lambda i}^0$ and $1/\delta_{\lambda i}$ are discussed in Sec. III.E.5.

Once the the optical depth due to collision broadening $\tau_{C\lambda i}$ and the optical depth due to Doppler broadening $\tau_{D\lambda i}$ are determined, their combined optical depth is calculated using

$$\tau_{\lambda i} = \left(1 - z_{\lambda i}^{-(1/2)} \right)^{1/2} \tau_{\lambda i}^* \quad (36)$$

where

$$z_{\lambda i} = \left[1 - \left(\frac{\tau_{C\lambda i}}{\tau_{\lambda i}^*} \right)^2 \right]^{-2} + \left[1 - \left(\frac{\tau_{D\lambda i}}{\tau_{\lambda i}^*} \right)^2 \right]^{-2} - 1 \quad (37)$$

Lastly, the optical depth for all species (including soot) combined can be found simply using

$$\tau_{\lambda} = \sum_{\text{species}} \tau_{\lambda i} \quad (38)$$

For this module, only emitting species with mole fractions greater than 0.01 in typical composite motor plumes are considered in the calculation of optical depth. These species are H_2O , CO_2 , CO , and HCl . H_2 and N_2 do not emit in the infrared [13], and so their emission is not considered.

The parameters $\bar{\kappa}_{\lambda i}^0$ and $1/\delta_{\lambda i}$ and the SLG model are validated in several radiative test cases in Ch. 7 of Ludwig et al.'s work [16]. Comparisons of experimental absorptance, emissivity, and radiance data for CO_2 , H_2O , CO , and HCl with model predictions using the parameters are given, as well as a comparison of calculated and measured radiant emission for a CO_2 and H_2O mixture, with good agreement.

5. Surrogate Models for Single Line Group Parameters

In the single line group model, the mean absorption coefficient $\bar{\kappa}_{\lambda i}^0$ and the average line density $1/\delta_{\lambda i}$ are determined using lookup tables for each molecule within small wavelength bands at different temperatures [16]. However, in order to maintain compatibility with AeroSandbox (see Sec. II for more information on AeroSandbox model requirements), C^1 -continuous models for $\bar{\kappa}_{\lambda i}^0$ and $1/\delta_{\lambda i}$ are needed. It should be noted that C^1 -continuity is only needed with respect to temperature and not with respect to wavelength. This is because temperature is defined within the AeroSandbox optimization environment as a variable that must be implicitly solved by the optimizer, whereas wavelengths are selected explicitly as problem constants that do not need to be solved.

Differentiable, C^1 -continuous surrogate models for $\bar{\kappa}_{\lambda i}^0$ and $1/\delta_{\lambda i}$ were developed for each considered species (H_2O , CO_2 , CO , and HCl) to meet this gap. The data tables in Ref. [16] were digitized. Missing values in the data were interpolated before fitting, and zero values in the data were replaced with small but nonzero values. Differentiable, cubic splines were fit to the logarithm of the data using the `UnstructuredInterpolatedModel()` class described in Sec. II.C. For values of temperature and wavelength outside the data range, the surrogate model extrapolates values to the nearest model value at the boundary of the data range. An example of the surrogate models for $\bar{\kappa}_{\lambda i}^0$ and $1/\delta_{\lambda i}$ is shown for CO in Fig. 5. In the figure, points plotted with circles are data points given in the data tables in Ref. [16] and the curves are the output of the surrogate model in the given wavelength range for

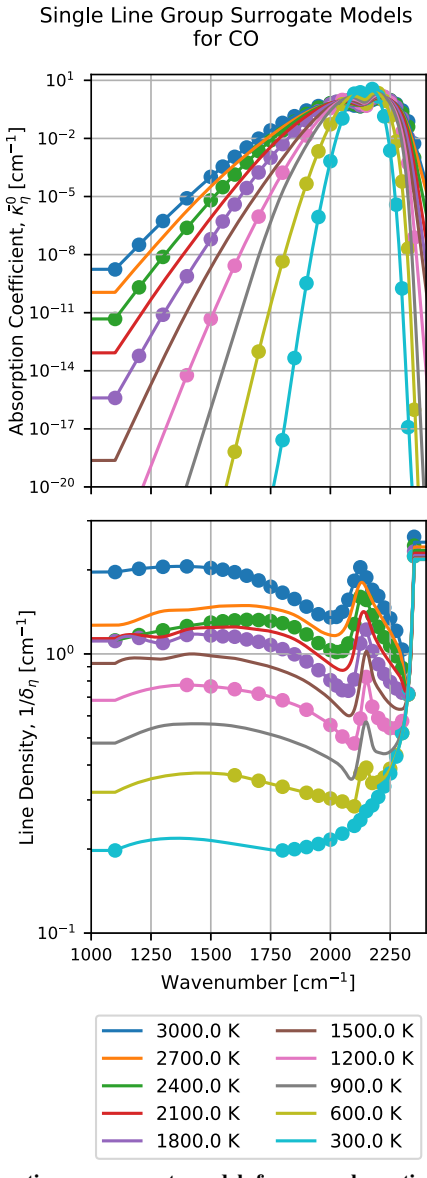


Fig. 5 C^1 -continuous surrogate models for mean absorption coefficient $\bar{\kappa}_{\eta i}^0$ and average line density $1/\delta_{\eta i}$. Plotted circles are data points given in Ref. [16], and curves are the output of the surrogate model.

selected temperatures. Plots of the surrogate models for the other molecules are available in Appendix C of Ref. [31].

IV. Results and Validation

The results of the previously described radiant intensity model are compared to different test cases to validate its performance. The model is compared to radiant intensity measurements for a collection of motor static fires of low-thrust (6 to 20 N), end-burning solid rocket motors operating at different chamber pressures and with varying amounts of the burn rate suppressant oxamide. Experimental measurements from a study conducted by Avital et al. [3]—which used a core-burning ballistic evaluation motor with an estimated ~ 1600 N thrust operated at sea level—are also compared to the developed radiant intensity model. Both the collection of low-thrust motor static fires and the Avital et al. measurements were calibrated so the effects of atmospheric absorption were eliminated.

A. Comparison with Low-Thrust, End-Burning Motor Experiments

The radiant intensity model is compared to measurements for a series of four static fires (SF-1—SF-4) of low-thrust (6 to 20 N), end-burning solid rocket motors, which are detailed in Ref. [32]. These motors have applications as propulsion for a class of kilogram-scale,

transonic aircraft, such as those described in Ref. [33]. The motors used an ammonium perchlorate composite propellant with a baseline propellant formulation consisting of 80% ammonium perchlorate and 20% hydroxyl-terminated polybutadiene based binder. The motors were operated at approximately 1.1 or 2.2 MPa, and the propellants were doped with 0% or 8% of the burn rate suppressant oxamide. The plume emittance was measured using a CI-Systems SR-5000N spectroradiometer with an average spectral resolution of ~ 0.02 μm . The experimental setup, motor design, and static fires are described further in Ref. [32]. The model input parameters are shown in Table 2, and the modeled and experimental results for radiant intensity are shown in Fig. 6.

Table 2 Radiant intensity model inputs for low-thrust, end-burning motors

Static fire	Oxamide, %	Throat diameter, mm	Chamber pressure, MPa	Exit pressure, MPa
SF-1	0	3.00	1.2	0.101
SF-2	0	2.30	2.3	0.101
SF-3	8	2.53	1.1	0.101
SF-4	8	1.93	2.1	0.101

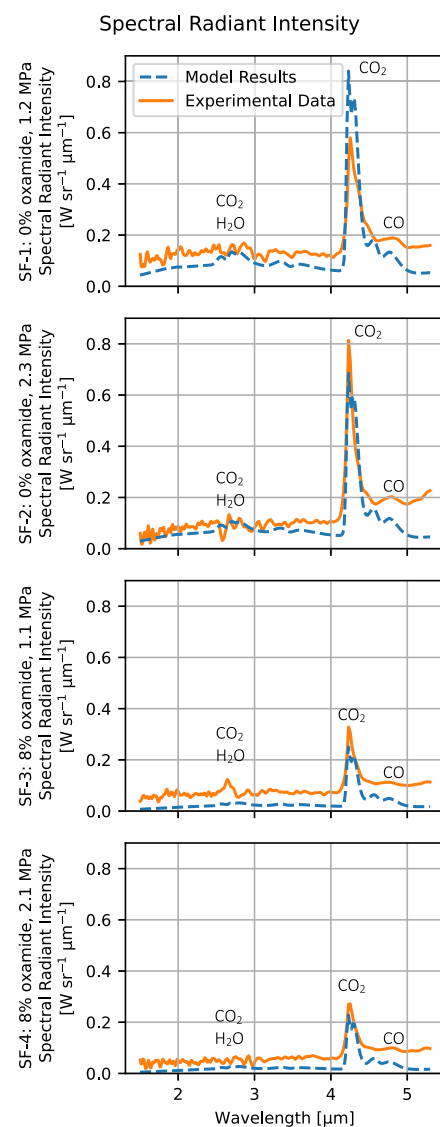


Fig. 6 Comparison of measured and modeled radiant intensities for SF-1 through SF-4.

The oxamide fraction and throat diameter were the actual values used in the experiments. The internal ballistics model described in Sec. III.B was not used, and instead the chamber pressures were set to the approximate steady-state values measured during the experiments. The exit pressure was assumed to be 0.101 MPa (standard sea level pressure) for all the static fires, which was the exit pressure for which each of the nozzles were designed. An altitude of 0 km and a freestream velocity of $1 \text{ m} \cdot \text{s}^{-1}$ was also used. A soot mass fraction of 0.02 was assumed. This is slightly higher than the mass fraction of 0.0135 reported by Vernacchia in Ref. [34] for these propellants; however, the reported value was a lower bound because some soot escaped during the measurements. The flow field was integrated to a distance of $60d_0$ (d_0 is the initial plume diameter at the start of the turbulent mixing region, as introduced in Sec. III.C.2) downstream of the start of the turbulent mixing region, assuming a viewing angle of 90° (e.g., orthogonal to the plume axis of symmetry, as was the measurement condition). A spectral resolution of $0.02 \mu\text{m}$ and a spatial resolution of $0.1d_0$ were used in the model for each test configuration. The d_0 for each of the test configurations varies slightly but is in the range of 3.6 to 4.7 mm.

For all four static fires, both the measured and modeled spectra show a distinct peak at $4.3 \mu\text{m}$ corresponding to CO_2 emission. A CO emission band can be seen at $4.7 \mu\text{m}$, although in the experimental data it appears as a relatively smooth plateau for all the static fires, whereas in the model it appears as two small peaks. A weaker peak exists at $2.7 \mu\text{m}$ corresponding to a combined CO_2 and H_2O emission band, although it is not particularly visible in the experimental data. The measured data and modeled results show reasonable agreement across the spectrum for all four static fires, although the measured experimental data are unfortunately noisy across the spectrum, especially away from the $4.3 \mu\text{m}$ CO_2 peak where the measured signal was weak.

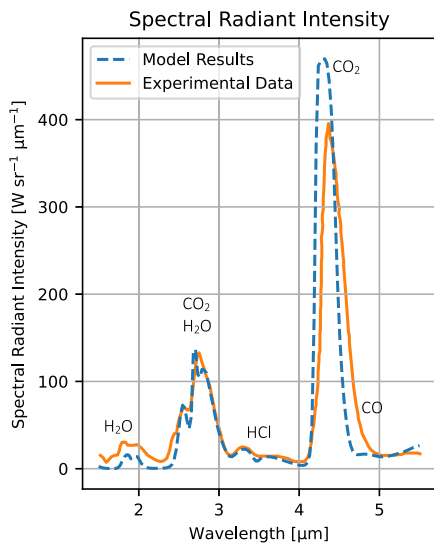


Fig. 7 Comparison between radiant intensity spectra for Avital et al. experimental results and the developed model.

B. Comparison with Avital et al. Ballistic Evaluation Motor Experiment

The developed radiant intensity model was compared to experimental data collected for a $\sim 1600 \text{ N}$ thrust test motor by Avital et al. in Ref. [3]. The test used a core-burning propellant grain consisting of 87% ammonium perchlorate oxidizer and 13% hydroxyl-terminated polybutadiene binder. The nozzle had a throat diameter of 15 mm, a chamber pressure of 3.8 MPa, and a nozzle exit pressure of 0.27 MPa. The emittance was measured using a CI-Systems SR-5000 spectroradiometer with an average spectral resolution of $\sim 0.02 \mu\text{m}$. The plume was integrated to a downstream distance of $26d_0$, which is consistent with the detector field of view and distance to detector used by Avital et al. A spectral resolution of $0.02 \mu\text{m}$ and a spatial resolution of $0.13d_0$, or $\sim 4.7 \text{ mm}$, was used in the radiant intensity model. The experimental radiant intensity data given by Avital et al. in Ref. [3] are plotted with the output of the radiant intensity model (using the motor parameters described previously) in Fig. 7.

The agreement between the model and the Avital et al. experimental radiant intensity spectra is good. The model performs quite well for the $3.5 \mu\text{m}$ HCl and the $2.7 \mu\text{m}$ combined H_2O and CO_2 bands and slightly underpredicts the emittance for the $1.87 \mu\text{m}$ H_2O band. The slight underprediction of the model at the smaller wavelengths is likely due to the presence of a small fraction of soot in the exhaust that is not accounted for in the model, which would lead to a small broadband increase in the radiant intensity at smaller wavelengths. Some of these bands were not visible in the radiant intensity data or model results for the SF-1—SF-4 static fires shown in Fig. 6 due to the low temperatures and small size scales of those plumes. The model overpredicts the $4.3 \mu\text{m}$ CO_2 peak radiant intensity by $\sim 19\%$. The center of the $4.3 \mu\text{m}$ CO_2 band between the model and Avital et al. measurement also differs, with the model predicting the band center near $4.31 \mu\text{m}$ and the data showing the center near $4.37 \mu\text{m}$. The single line group model (discussed in Sec. III.E.4) used for modeling molecular emission predicts the CO_2 band center very near $4.31 \mu\text{m}$. It is not known why the model and Avital et al. band centers differ.

V. Optimization Case Study for a Small, Low-Thrust Solid Rocket Motor

A. Design Problem Setup

To demonstrate the utility of the end-to-end differentiable radiant intensity model, this section provides an example case study for optimizing a solid rocket-powered vehicle using the model and the AeroSandbox design optimization framework. As an example, consider a kilogram-scale, transonic aircraft concept propelled with a low-thrust, end-burning solid rocket motor, as illustrated in Fig. 8 (similar to the aircraft concept introduced in Ref. [33]). The vehicle concept uses an end-burning motor with a fixed burn area that delivers a constant thrust. The motors used an ammonium perchlorate composite propellant with a baseline propellant formulation consisting of 80% ammonium perchlorate and 20% hydroxyl-terminated polybutadiene based binder. The baseline propellant formulation can be diluted with some mass fraction y_{om} of oxamide burn rate suppressant. The chamber pressure of the motor can be manipulated by changing the nozzle throat diameter d_t .

A possible vehicle design might have a goal of maximizing the vehicle specific impulse (which maximizes vehicle burn time). It

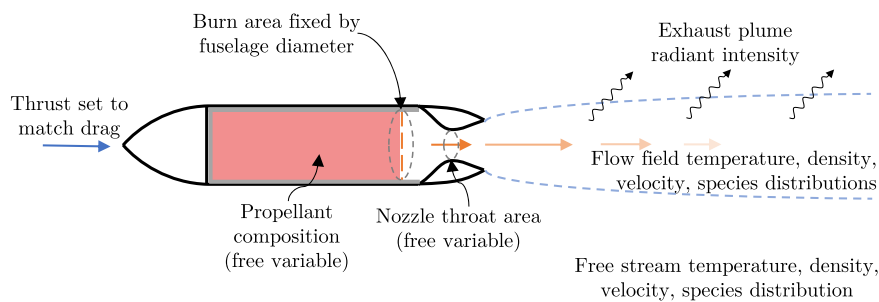


Fig. 8 Low-thrust, transonic aircraft concept.

could also be of interest to constrain the radiant emission in the $4.3 \mu\text{m}$ CO_2 band to be less than some target value if vehicle visibility is a concern. Two design optimization scenarios are considered in this case study. The first design scenario optimizes vehicle specific impulse with no constraint on radiant intensity (the *unconstrained* design). The second scenario optimizes specific impulse subject to a constraint that the radiant intensity at $4.3 \mu\text{m}$ is less than $0.1 \text{ W} \cdot \text{sr}^{-1} \cdot \mu\text{m}^{-1}$ (the *constrained* design).

These scenarios can be formulated as design optimization problems and can be defined using the appropriate problem variables, constraints, and objective for implementation in AeroSandbox (see Sec. II for a discussion of AeroSandbox). The problem elements for these case study scenarios are summarized subsequently.

Constraints:

- 1) Thrust, $F = 15 \text{ N}$
- 2) Burn area, $A_b = 2500 \text{ mm}^2$
- 3) Altitude, $H = 10 \text{ km}$
- 4) Freestream velocity, $u_\infty = \text{Mach } 0.8 \approx 240 \text{ m} \cdot \text{s}^{-1}$
- 5) Propellant oxamide mass fraction, $0 \leq y_{\text{om}} \leq 0.2$
- 6) Radiant intensity, $J_{\lambda=4.3\mu\text{m}}$
 - a) Unconstrained design: no constraint on $J_{\lambda=4.3\mu\text{m}}$
 - b) Constrained design: $J_{\lambda=4.3\mu\text{m}} \leq 0.1 \text{ W} \cdot \text{sr}^{-1} \cdot \mu\text{m}^{-1}$

Variables:

- 1) Nozzle throat diameter, d_t
- 2) Propellant oxamide mass fraction, y_{om}

Objective:

- 1) Maximize specific impulse, I_{sp}

Both scenarios were implemented in AeroSandbox with the additional constraints imposed by the six submodels for modeling plume radiant emission discussed in Sec. III. For the internal ballistics submodel, the propellant burn rate coefficient a was defined as a function of the propellant oxamide mass fraction y_{om} and the propellant burn rate exponent was treated as constant following the model and treatment in Ref. [27]. The design problems were solved to determine the nozzle throat diameter and propellant oxamide mass fraction that maximized specific impulse subject to the constraints.

B. Results

The scenarios described in the previous subsection were optimized using AeroSandbox to determine the maximum specific impulse design. The optimized design and performance parameters are summarized in Table 3.

The constrained and unconstrained designs have very different $J_{\lambda=4.3\mu\text{m}}$ values. The unconstrained design has $J_{\lambda=4.3\mu\text{m}} = 0.14 \text{ W} \cdot \text{sr}^{-1} \cdot \mu\text{m}^{-1}$. The constrained design has $J_{\lambda=4.3\mu\text{m}} = 0.10 \text{ W} \cdot \text{sr}^{-1} \cdot \mu\text{m}^{-1}$, which is significantly smaller than the unconstrained design. The value is also at the boundary of the $J_{\lambda=4.3\mu\text{m}} \leq 0.1 \text{ W} \cdot \text{sr}^{-1} \cdot \mu\text{m}^{-1}$, and so this constraint drives this design. The reduced $J_{\lambda=4.3\mu\text{m}}$ in the constrained design is achieved by operating the motor at a higher oxamide content w_{om} and higher chamber pressure p_c (which is set by a smaller throat diameter d_t) than the unconstrained design. It should also be noted that the constrained design (along with the unconstrained design) is feasible for this class of propellants. Static fire and minimum combustion pressure measurements collected by Vernacchia et al. for this class of propellants showed that motors of this size scale can have stable

Table 3 Comparison of vehicle design and performance parameters for small, low-thrust aircraft scenarios

	Unconstrained	Constrained, $J_{\lambda=4.3\mu\text{m}} \leq 0.1 \text{ W} \cdot \text{sr}^{-1} \cdot \mu\text{m}^{-1}$
Oxamide content, $y_{\text{om}} [-]$	0.126	0.155
Throat diameter, $d_t [\text{mm}]$	3.24	2.71
Chamber pressure, $p_c [\text{MPa}]$	1.20	1.68
Radiant Intensity at $4.3 \mu\text{m}$, $J_{\lambda=4.3\mu\text{m}} [\text{W} \cdot \text{sr}^{-1} \cdot \mu\text{m}^{-1}]$	0.14	0.10
Specific impulse, $I_{\text{sp}} [\text{s}]$	184	183

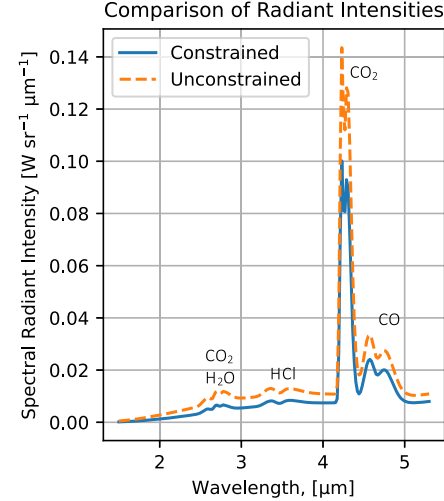


Fig. 9 Comparison of radiant intensities of unconstrained and constrained designs.

combustion at oxamide contents up to 20% for chamber pressures above $\sim 0.4 \text{ MPa}$ [27]. Both these designs are far away from these operational limits.

Despite the significant differences in peak radiant intensity, oxamide content, chamber pressure, and throat diameter, the specific impulse is nearly identical between the two designs. Including the $J_{\lambda=4.3\mu\text{m}} \leq 0.1 \text{ W} \cdot \text{sr}^{-1} \cdot \mu\text{m}^{-1}$ constraint for this design problem incurs almost no specific impulse performance penalty. The developed radiant intensity model enables the direct optimization of this constrained design and revealed for this case study a new design that reduces plume radiant intensity and maintains a nearly identical specific impulse.

The predicted radiant intensities for the constrained and unconstrained designs are shown in Fig. 9. The emission for the constrained design is smaller across the spectrum than the unconstrained design. This is expected given the driving $J_{\lambda=4.3\mu\text{m}} \leq 0.1 \text{ W} \cdot \text{sr}^{-1} \cdot \mu\text{m}^{-1}$ constraint, which selects for a higher oxamide content design with significantly smaller motor chamber and nozzle exit temperatures which reduces emission everywhere. The emission spectra show distinct peaks for the $2.7 \mu\text{m}$ combined H_2O and CO_2 band, the $3.5 \mu\text{m}$ HCl band, the $4.3 \mu\text{m}$ CO_2 band, and the $4.7 \mu\text{m}$ CO band. The emission for both designs is still relatively weak, due to the small vehicle size, high propellant oxamide content, low propellant mass flow rate, and low ambient pressure and species concentrations at 10 km altitude.

VI. Conclusion

For vehicles where visibility is important, considering plume radiant emission during the design phase is important for ensuring vehicle design constraints and objectives can be met while accounting for the coupling of plume radiant emission with other aspects of vehicle design. In this paper, an end-to-end differentiable model coupling solid rocket motor design parameters to exhaust plume radiant emission was developed. The model is compatible with automatic differentiation and gradient-based optimizers and was specifically implemented in the AeroSandbox aircraft design optimization framework. To the author's knowledge, no previous study in the open literature has developed and demonstrated a radiant emission model that is compatible with automatic differentiation and gradient-based optimizers.

The developed differentiable model consists of six submodels of different coupled physical phenomena: chamber thermodynamic equilibrium, motor internal ballistics, isentropic nozzle flow, plume flow field, afterburning kinetics, and radiative transfer. The developed model shows reasonable agreement for a number of motors, and its functionality was demonstrated for an optimization case study with a low-thrust, transonic rocket-powered aircraft concept. Further model development should expand the types of propellants and

operating conditions that can be modeled and provide options to account for atmospheric absorption and to evaluate spatially resolved radiant quantities. An improved kinetics model should also be considered so that reaction rates can more accurately and robustly be predicted, especially at higher altitudes where the reduced-order model presented in this paper performs poorly. The model development work in this paper enables the direct optimization of rocket-powered vehicles with constraints on radiant emission, supporting a better understanding of motor design and performance tradeoffs and improved motor performance.

Acknowledgments

This work was funded by BAE Systems, Inc.

References

- [1] Sharpe, P., "AeroSandbox: A differentiable Framework for Aircraft Design Optimization," SM Thesis, Massachusetts Inst. of Technology, Cambridge, MA, 2021, <https://dspace.mit.edu/handle/1721.1/140023>.
- [2] Niu, Q., He, Z., and Dong, S., "IR Radiation Characteristics of Rocket Exhaust Plumes Under Varying Motor Operating Conditions," *Chinese Journal of Aeronautics*, Vol. 30, No. 3, 2017, pp. 1101–1114. <https://doi.org/10.1016/j.cja.2017.04.003>
- [3] Avital, G., Cohen, Y., Gamss, L., Kanelbaum, Y., Macales, J., Trieman, B., Yaniv, S., Lev, M., Stricker, J., and Sternlieb, A., "Experimental and Computational Study of Infrared Emission from Underexpanded Rocket Exhaust Plumes," *Journal of Thermophysics and Heat Transfer*, Vol. 15, No. 4, 2001, pp. 377–383. <https://doi.org/10.2514/2.6629>
- [4] Devir, A., Lessin, A., Cohen, Y., Yaniv, S., Kanelbaum, Y., Avital, G., Gamss, L., Macales, J., Trieman, B., Lev, M., et al., "Comparison of Calculated and Measured Radiation from a Rocket Motor Plume," *39th Aerospace Sciences Meeting and Exhibit*, AIAA Paper 2001-0358, 2001. <https://doi.org/10.2514/6.2001-358>
- [5] Zhang, X., and Li, R., "Numerical Study on Similarity of Plume's Infrared Radiation from Reduced Scaling Solid Rocket," *Journal of Applied Mathematics*, Vol. 2015, No. 1, 2015, Paper 627351. <https://doi.org/10.1155/2015/627351>
- [6] Stowe, R., Ringuette, S., Fournier, P., Smithson, T., Pimentel, R., Alexander, D., and Link, R., "Effect of Flight and Motor Operating Conditions on IR Signature Predictions of Rocket Exhaust Plumes," *International Journal of Energetic Materials and Chemical Propulsion*, Vol. 14, No. 1, 2015, pp. 29–56. <https://doi.org/10.1615/IntJEnergeticMaterialsChemProp.2015011502>
- [7] Rialland, V., Guy, A., Gueyffier, D., Perez, P., Roblin, A., and Smithson, T., "Infrared Signature Modelling of a Rocket Jet Plume—Comparison with Flight Measurements," *Journal of Physics: Conference Series*, Vol. 676, No. 1, 2016, Paper 012020. <https://doi.org/10.1088/1742-6596/676/1/012020>
- [8] Kim, S., Kim, S., Kim, M., Song, S., and Lee, J. S., "Infrared Signature of NEPE, HTPB Rocket Plume Under Varying Flight Conditions and Motor Size," *Infrared Physics & Technology*, Vol. 112, Jan. 2021, Paper 103590. <https://doi.org/10.1016/j.infrared.2020.103590>
- [9] Wang, W., Li, S., Zhang, Q., and Wang, N., "Infrared Radiation Signature of Exhaust Plume from Solid Propellants with Different Energy Characteristics," *Chinese Journal of Aeronautics*, Vol. 26, No. 3, 2013, pp. 594–600. <https://doi.org/10.1016/j.cja.2013.04.019>
- [10] Niu, Q., Fu, D., Dong, S., and Tan, H., "A Simplified Model for Fast Estimating Infrared Thermal Radiation of Low-Altitude Under-Expanded Exhaust Plumes," *International Journal of Heat and Mass Transfer*, Vol. 136, June 2019, pp. 276–287. <https://doi.org/10.1016/j.ijheatmasstransfer.2019.03.003>
- [11] Woodroffe, J., "One-Dimensional Model for Low-Altitude Rocket Exhaust Plumes," *13th Aerospace Sciences Meeting*, AIAA Paper 1975-0244, 1975. <https://doi.org/10.2514/6.1975-244>
- [12] Rialland, V., Nicole, A., Alomar Sitjes, A., Guy, A., and Lefèvre, S., "Ballistic Missile Infrared Signatures: Towards a Surrogate Model," *OPTRO 2020*, 2020, <https://hal.archives-ouvertes.fr/hal-02486779>.
- [13] Simmons, F. S., *Rocket Exhaust Plume Phenomenology*, Aerospace Press, El Segundo, CA, 2000, pp. 39–42, 113–117. <https://doi.org/10.2514/4.989087>
- [14] Mao, H., Fu, D., and Bao, X., "Engineering Method of Predicting Rocket Exhaust Plumes at Middle and Low Altitudes," *Journal of Spacecraft and Rockets*, Vol. 54, No. 5, 2017, pp. 1170–1177. <https://doi.org/10.2514/1.A33597>
- [15] Modest, M. F., *Radiative Heat Transfer*, 3rd ed., Academic Press, Amsterdam; Boston, 2003, pp. 303–369 (Chap. 11), 418–426. <https://doi.org/10.1016/B978-0-12-503163-9.X5000-0>
- [16] Ludwig, C. B., Malkmus, W., Reardon, J. E., and Thomson, J. A. L., "Handbook of Infrared Radiation from Combustion Gases," NASA SP-3080, 1973.
- [17] Andersson, J. A. E., Gillis, J., Horn, G., Rawlings, J. B., and Diehl, M., "CasADi: A Software Framework for Nonlinear Optimization and Optimal Control," *Mathematical Programming Computation*, Vol. 11, No. 1, 2019, pp. 1–36. <https://doi.org/10.1007/s12532-018-0139-4>
- [18] Wächter, A., and Biegler, L. T., "On the Implementation of an Interior-Point Filter Line-Search Algorithm for Large-Scale Nonlinear Programming," *Mathematical Programming*, Vol. 106, No. 1, 2006, pp. 25–57. <https://doi.org/10.1007/s10107-004-0559-y>
- [19] Baydin, A. G., Pearlmutter, B. A., Radul, A. A., and Siskind, J. M., "Automatic Differentiation in Machine Learning: A Survey," *Journal of Machine Learning Research*, Vol. 18, No. 53, 2018, pp. 1–43. <https://doi.org/10.48550/arXiv.1502.05767>
- [20] Ponomarenko, A., "RPA: Tool for Liquid Propellant Rocket Engine Analysis C++ Implementation," RP Software+Engineering UG TR, Neunkirchen-Seelscheid, Germany, 2010.
- [21] McBride, B. J., Zehe, M. J., and Gordon, S., "NASA Glenn Coefficients for Calculating Thermodynamic Properties of Individual Species," NASA Glenn Research Center TP-2002-211556, Sept. 2002, <https://ntrs.nasa.gov/citations/20020085330>.
- [22] Sutton, G. P., and Biblarz, O., *Rocket Propulsion Elements*, 8th ed., Wiley, Hoboken, NJ, 2010, p. 418.
- [23] Vernacchia, M. T., "proptools: Rocket Propulsion Design Tools," 2017, <https://proptools.readthedocs.io/en/latest/>
- [24] Witze, P. O., "Centerline Velocity Decay of Compressible Free Jets," *AIAA Journal*, Vol. 12, No. 4, 1974, pp. 417–418. <https://doi.org/10.2514/3.49262>
- [25] Goodwin, D. G., Speth, R. L., Moffat, H. K., and Weber, B. W., "Cantera: An Object-Oriented Software Toolkit for Chemical Kinetics, Thermodynamics, and Transport Processes," 2021, <https://www.cantera.org>.
- [26] Ecker, T., Karl, S., and Hannemann, K., "Combustion Modeling in Solid Rocket Motor Plumes," EUCASS (European Conference for Aerospace Sciences), Brussels, Belgium, 2019, p. 17. <https://doi.org/10.13009/EUCASS2019-79>
- [27] Vernacchia, M. T., Mathesius, K. J., and Hansman, R. J., "Slow-Burn Ammonium Perchlorate Propellants with Oxamide: Burn Rate Model, Testing, and Applications," *Journal of Propulsion and Power*, Vol. 37, No. 5, 2021, pp. 792–800. <https://doi.org/10.2514/1.B38106>
- [28] Newville, M., Stensitzki, T., Allen, D. B., and Ingargiola, A., "LMFIT: Non-Linear Least-Square Minimization and Curve-Fitting for Python," Sept. 2014. <https://doi.org/10.5281/zenodo.11813>
- [29] Howell, J. R., Siegel, R., and Mengüç, M. P., *Thermal Radiation Heat Transfer*, 5th ed., CRC Press, Boca Raton, FL, 2011, pp. 518–526. <https://doi.org/10.1201/9781439894552>
- [30] Chang, H.-C., and Charalampopoulos, T. T., "Determination of the Wavelength Dependence of Refractive Indices of Flame Soot," *Proceedings of the Royal Society of London. Series A: Mathematical and Physical Sciences*, Vol. 430, No. 1880, 1990, pp. 577–591. <https://doi.org/10.1098/rspa.1990.0107>
- [31] Mathesius, K. J., "Integrated Design of Solid Rocket Powered Vehicles Including Exhaust Plume Radiant Emission," PhD Thesis, Massachusetts Inst. of Technology, Cambridge, MA, 2023, <https://dspace.mit.edu/handle/1721.1/151348>.
- [32] Mathesius, K. J., Knotts, M. E., Vernacchia, M. T., and Hansman, R. J., "Experimental Study of Low-Thrust, End-Burning Solid Rocket Motors Including Plume Radiant Emission," *Journal of Spacecraft and Rockets*, Aug. 2024 (Published Online). <https://doi.org/10.2514/1.A36028>
- [33] Vernacchia, M. T., Mathesius, K. J., and Hansman, R. J., "Low-Thrust Solid Rocket Motors for Small, Fast Aircraft Propulsion: Design and Development," *Journal of Propulsion and Power*, Vol. 38, No. 1, 2022, pp. 122–134. <https://doi.org/10.2514/1.B38104>
- [34] Vernacchia, M. T., "Development of Low-Thrust Solid Rocket Motors for Small, Fast Aircraft Propulsion," Ph.D. Thesis, Massachusetts Inst. of Technology, Cambridge, MA, 2020, <https://dspace.mit.edu/handle/1721.1/127069>.